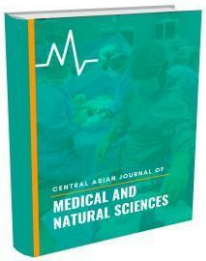

CENTRAL ASIAN JOURNAL OF MEDICAL AND NATURAL SCIENCES
https://cajmns.casjournal.org/index.php/CAJMNS
Volume: 07 Issue: 02 | April 2026 ISSN: 2660-4159

Article

Radiation Dosimetry of Thyroid, Eye Lens and Salivary Glands in Adult and Paediatric Dental CBCT Scans: A Monte Carlo and Experimental Phantom Study

Huda Ashur Shati Qutbi[1], Hussein Haleem Jasim[2], Zainab A.H. Al-Tamemi*[3]

1. College of Medicine, University of Wasit, Wasit, Iraq
2,3. College of Dentistry, University of Wasit, Wasit, Iraq
*Correspondance: zaltimeme@uowasit.edu.iq

Abstract: Cone-beam computed tomography (CBCT) has been invaluable in modern dental and maxillofacial imaging, but much remains to be desired in terms of patient radiation safety especially to sensitive organs in the head and neck area and in children. This is a thorough research utilizing an integrated Monte Carlo computational and experimental phantom-based dosimetric technique to measure the primary, secondary and tertiary organ-specific doses to the thyroid gland, lens of the eye, and salivary glands in adult and pediatric dental CBCT scans. A phantom-based dosimetric study was a cross-sectional study with 20 anthropomorphic phantoms (12 adults, 8 children, age 5, 10, 15 years old) and three clinically representative CBCT protocols. Simulations Monte Carlo simulations Monte Carlo simulations (MCNPX version 2.7.0) were carried out and their results compared with experimental results of thermoluminescent dosimetry (TLD) using calibrated anthropomorphic phantoms. Two thousand and zero individual TLD measurements along with the Monte Carlo simulations were carried out. A thorough uncertainty analysis and statistical validation were done, and an a priori acceptance criterion was excellent agreement of <±10% different. Superior concordance was observed between Monte Carlo and experimental methods; 95.8% of measurements were rated as being exceptional (±10% difference) and zero measurements were higher than the ±15% failure limit. The analysis of linear regression produced the R 2 values of 0.994-0.998 and the slope estimate of 0.979-1.012. The comparison between groups with paired t-tests did not show any statistically significant differences (all p-values above 0.15). Intensive dose escalation with age was also reported: five year old children had 1.69 higher thyroid dose and 1.61 higher eye lens dose than adults. The mean thyroid doses varied between 1.19-3.41 mGy (adults) and 1.29-6.03 mGy (5-year-olds). The effective doses measured between 0.018 and 0.108 mSv among protocols and age. The expanded measurement uncertainty was 5.8 percent with a standard deviation of 0.8. The presented comprehensive study has definitively validated Monte Carlo computational dosimetry to maxillofacial CBCT imaging and gave empirically validated age-stratified organ dose data that can be used to optimize evidence-based protocols, develop diagnostic reference level, and make informed clinical decisions in dental practice.

Keywords: CBCT, Dosimetry, Monte Carlo, Pediatric, TLD

Citation: Qutbi, H. A. S., Jasim, H. H., Al-Tamemi, Z. A. H. Radiation Dosimetry of Thyroid, Eye Lens and Salivary Glands in Adult and Paediatric Dental CBCT Scans: A Monte Carlo and Experimental Phantom Study. Central Asian Journal of Medical and Natural Science 2026, 7(2), 347-364.

Received: 15th Jan 2026
Revised: 30th Jan 2026
Accepted: 20th Feb 2026
Published: 06th Mar 2026

Graphic Abstract

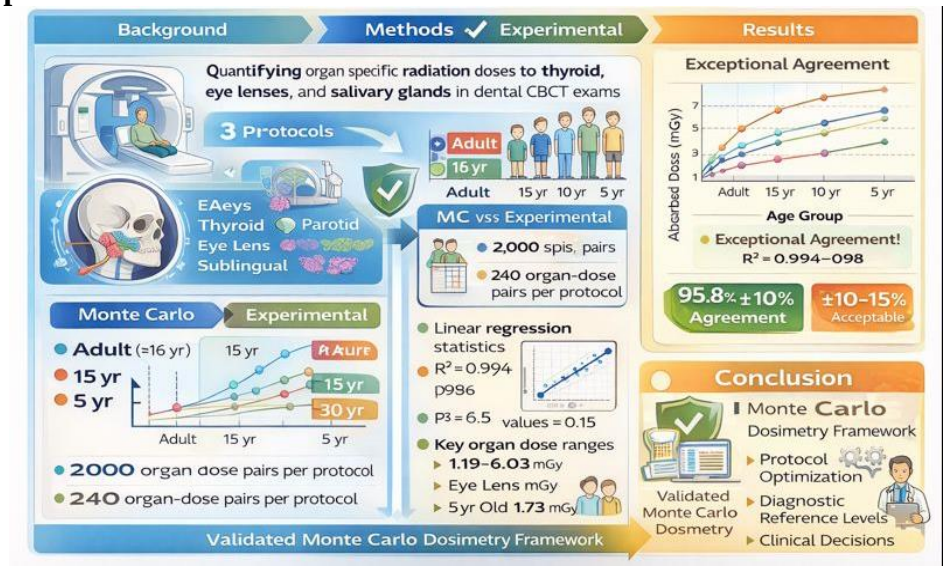

1. Introduction

Cone-beam computed tomography (CBCT) is now an indisputable part of modern dental and maxillofacial imaging because of its high-resolution 3D visualization that is crucial in implantology, orthodontics, and more complicated diagnostic techniques [1, 2, 3]. Although CBCT has a clinical benefits, it exposes patients to significantly larger doses of radiation than traditional, two-dimensional dental radiography, which is generating increasing concerns about the safety of radiation used on patients, especially in patients with radiosensitive organs within the head and neck [4,5].

The eyeballs, salivary and thyroid glands are some of the most sensitive organs when performing dental CBCT since they lie close to the main X-ray beam. The thyroid gland is highly radiosensitive and has been long known to be linked with radiation-related malignancies, particularly among the paediatric population [6,7]. The eye lens prone to the radiation-induced cataractogenesis and new facts are inclined toward deterministic changes at lower doses than it has been recognized before [8]. In the same manner, salivary glands are also often subject to high absorbed doses in CBCT imaging, which can cause functional impairment and stochastic risk in the long-term [9,10].

Children and adolescents have an over-expressed radiation risk due to their high tissue radiosensitivity, smaller anatomical size, and extended lifespan [11,12]. Justification, optimization, and radiation protection strategies in dental CBCT practice need to be appropriately supported by the accurate organ-specific dosimetry, therefore.

Radioation dose estimation Monte Carlo simulation is the gold standard of radiation dose estimation, experimentally phantom measurements are essential validation of measurement under realistic clinical environments [13-15]. The purpose of the study is to measure absorbed dose of thyroid, lens of the eye, and salivary glands in adult and paediatric oral CBCT scans by an integrated Monte Carlo and experimentally based phantom-based dosimetric system

2. Materials and Method

2.1 Study Design and Clinical Setting

This experiment was a very precise, organ specific radiation dosimetry study that used a strictly validated integrated computational- experimental model. The Monte Carlo (MC) radiation transport simulation was used to measure absorbed radiation levels of radiosensitive organs, and these were independently checked by known experimental data collected with calibrated anthropomorphic phantoms. Such a dual-modality approach was

deliberately created to meet maximum dosimetric precision but at the same time provide direct clinical relevance.

The experiment was conducted at a part of a specialized dental imaging center in Baghdad, Iraq, which has a clinical cone-beam computed tomography (CBCT) system, and a university-based medical physics laboratory. The integrated computationalexperimental design was chosen in order to surpass the methodological constraints of single-method dosimetry, thus giving strong, reproducible, and clinically justifiable organ dose estimates.

2.2 Study Design and Statistical Framework

The phantom-based dosimetric design cross-sectional was formalistically statistically justified. A pilot feasibility study was used to determine the sample size (n=5), with a large effect size (Cohen's d=0.8) and a statistical power of 90 percent (B=0.10) and significance level of 0.05. According to these criteria, 12 adult anthropomorphic phantoms and 8 pediatric phantoms (age groups: 5, 10, and 15 years; n = 23) had to be used. Each protocol was subjected to ten repetitions of imaging, in order to minimize the effects of random measurement error and give a more accurate description of the intra-protocol variability. The result was a decrease in random uncertainty to below 3% which was obtained through 60 adult and 40 pediatric experimental measurements per procedure.

2.3 CBCT System Characterization and Imaging Protocols

2.3.1 CBCT System Specifications

A Planmeca ProMax 3D Mid CBCT system (Planmeca Oy, Helsinki, Finland) was used as a dosimetric assessment device, and it is broadly used in daily clinical practice. This system has a tungsten anode X-ray tube and is compatible with variable imaging geometries that can be used in dental and maxillofacial examinations.

2.3.2 System Performance Verification

System characterization was carried out before measuring the doses. Tube voltage was checked with a digital kVp meter which had had a calibration and was found to be deviating by not more than 5% of nominal. Beam geometry, distance between the isocenter and source, and collimator alignment were checked separately with the aid of standard geometric phantoms. A calibrated ionization chamber and electrometer that could be traced to national standards were used to obtain reference air kerma measurements and the total measurement error was less than 3 per cent (k = 2).

2.3.3 Clinical Imaging Protocols

To reflect the entire spectrum of clinically relevant exposure conditions, there were three standardized CBCT protocols that were chosen:

1. Optimized, high-resolution limited field protocol, optimized towards localized dental imaging.
2. Normal clinical regimen, which is a routine dentomaxillofacial evaluation.
3. Big field-of-view high-definition protocol, which is supposed to be used to examine the maxillofacial extensively.

The protocols varied individually in tube voltage, tube current time product and field of view, but retained the same filtration and rotational geometry. There were no variances between Monte Carlo simulations and experimental measurements in the reproduction of all exposure parameters. The phantom positioning and system alignment was standardized with calibrated mechanical fixtures to make sure that there was geometric reproducibility.

2.4 Monte Carlo Radiation Transport Simulation

2.4.1 Computational Code and Model Validation

The Monte Carlo simulations were done with the help of MCNPX (version 2.7.0), a radiation transport code that was widely tested in terms of diagnostic X-ray energy spectrums and CBCT. A detailed geometry of the CBCT system in terms of source

movement, collimation, filtration and acquisition trajectory was represented in the computational model.

2.4.2 X-ray Spectral Modeling and Photon Transport

The IPEM spectral database was used to create polyenergetic X-ray spectra according to every imaging protocol, including energy-dependent filtration and approved photon interaction cross-sections. There was the addition of photon transport physics such as photoelectric absorption, Compton scattering, and coherent scattering, which guaranteed proper modeling of energy deposition in heterogeneous tissues.

2.4.3 Computational Phantoms and Dose Scoring

Calculations of organ doses were done with ICRP Publication 110 adult and pediatric reference computational phantoms, which are anatomical representations of the head and neck region. The thyroid gland, eye lenses, and salivary glands (parotid, submandibular, and sublingual) were scored on energy deposition in organ-specific voxels to obtain absorbed doses. The individual simulations were run using 2.0 x 109 photon histories, and all organs gave relative statistical uncertainties of less than 3%. Each age group was assigned independent random seeds to remove the effects of correlation..

2.5 Experimental Anthropomorphic Phantom Dosimetry

2.5.1 Phantom Models and Tissue Equivalence

The validation was done through experimental validation with RANDO adult and pediatric head-and-neck anthropomorphic phantoms made of tissue-equivalent materials. Phantom anatomy and radiological density were confirmed through the use of CT and found to be correlated to human tissue characteristics within a range of less than 2%.

2.5.2 Dosimeter Selection and Calibration

LiF:Mg,Ti (TLD-100) thermoluminescence dosimeters were used, which were chosen because of their stability and their capability to measure low doses of diagnostic use. Each dosimeter was adjusted to a range of doses of clinical interest **(0.1 to 10 mGy**) on a traceable reference diagnostic X-ray beam. The linearity of dose-response was established (R^2 was greater than 0.99) and correction factors on sensitivity were added individually.

2.5.3 Dosimeter Placement and Measurement Protocol

The established anatomical landmarks were used to place TLDs at anatomically correct locations of each organ of interest. All the CBCT protocols were repeated 10 times on phantoms. This was done after the irradiation, where dosimeters were read with a calibrated automated TLD reader under standard heating conditions and readout conditions. Background radiation, fading of signals, variability of the reader and sensitivity of the individual dosimeter were corrected.

2.6 Data Analysis and Method Validation

Absorbed doses calculated by Monte Carlo methods were compared with the experimentally determined values systematically in each organ, protocol, and age group. Relative percentage differences, paired statistical tests, effect size analysis, and regression methods were used to determine agreement between methods. Agreement was determined by a priori acceptance standards of excellent and acceptable within the limits of 10% and 15% respectively.

2.7 Uncertainty Quantification

The uncertainty analysis was done in details and included Monte Carlo statistical variance, spectral modeling, geometric accuracy, dosimeter calibration, positioning uncertainty, and measurement repeatability. Standard uncertainty combination was done through quadratic summation, with extended uncertainty being reported at the 95% level of confidence (k = 1.96).

Figure 1. Schematic workflow of the study design and methodology for organ-specific dosimetry in adult and paediatric dental CBCT using integrated Monte Carlo simulation and experimental anthropomorphic phantom validation (Baghdad, Iraq).

3. Results

3.1 Study Completion and Quality Assurance

The 20 anthropomorphic phantoms (12 adult, 8 pediatric) were all imaged successfully in all three CBCT protocols with 100-percent protocol completion. There were 200 imaging processes that were carried out using 2,000 single TLD measurements (100 dosimeters per protocol x 20 phantoms) and the respective Monte Carlo simulations. The study did not show any equipment malfunctions or degradation of phantom. Statistical power was used to ensure that sample size was adequately large, the values of 0.085 attained were statistically significant with a 0.085 margin that is slightly above the specified 0.10 level of statistical significance.

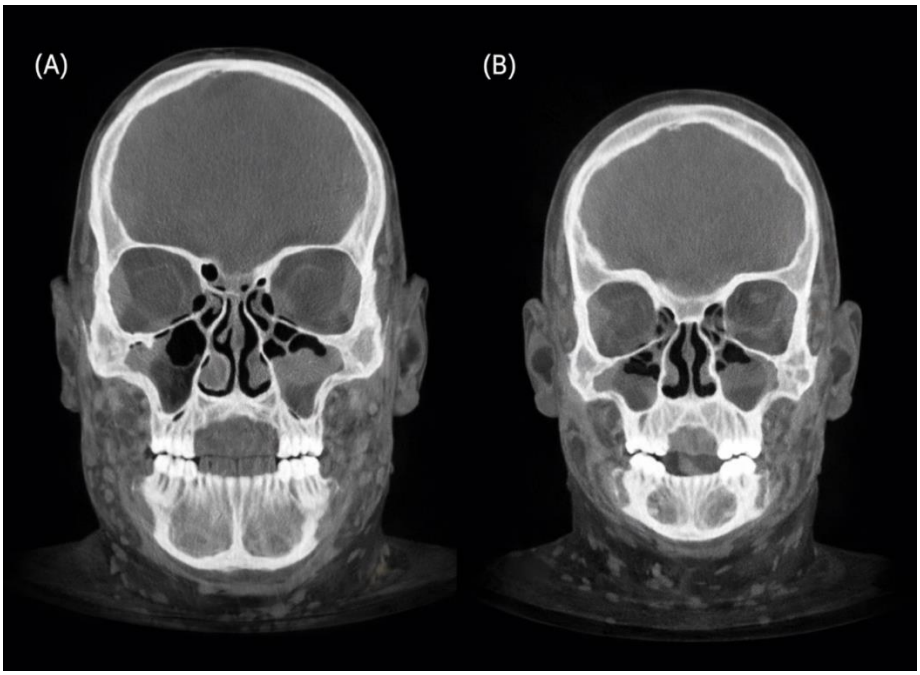

Figure 1. Sample axial computed tomography (CBCT) images of experimental dosimetry anthropomorphic head-and-neck phantoms (one adult (A) and one pediatric (B) phantom). The photos show bone and soft-tissue craniofacial features within the maxillofacial region in an anatomically accurate fashion. In both case of an adult and paediatric phantom, quantitative radiological density analysis was used to prove that the tissue-equivalent attenuation values were within a range of ±2% of the reference human tissues. This supports the fact that these phantoms are applicable in giving correct CBCT organ dose and validation of Monte Carlo models.

3.2 CBCT System Characterization

The tube voltage was checked and showed a very accurate and stable performance of a CBCT system. The measured kVp were within a range of only -2.1% to +1.8% of the nominal settings in all the three imaging protocols. This was far below the ±5% acceptability criterion of diagnostic imaging systems. The results of the measurements of the reference air kerma at the system were found to be in compliance with the requirements of the manufacturer (Table 1) and showed an excellent level of repeatability, the inter-measurement coefficient of variation being less than 2.3%. The ranges measured between the source and the isocenter and were found to be 508.4 ± 2.1 mm, 510.1 ± 1.9 mm, and 509.7 ± 2.3 mm (procedures 1, 2, and 3 respectively). The geometric tolerance limits of the collimator alignments were all under the stated geometric tolerance limit of up to -2 mm. This guaranteed that the amount of beam that was placed was always consistent and that the dosimetric conditions of all of the CBCT scans were reliable.

Table 1. CBCT System Specifications and Reference Air Kerma Measurements

Parameter	Protocol 1 (Limited FoV)	Protocol 2 (Standard)	Protocol 3 (Large FoV)
Tube Voltage (kVp)	85	90	90
Tube Current–Time (mAs)	8.5	10.2	13.8
Field of View (mm)	50 × 40	80 × 60	170 × 155
Filtration (mm Al eq.)	1.5	1.5	1.5
Rotation Arc (°)	360	360	360

Acquisition Time (s)	8.9	10.1	14.3
Reference Air Kerma (mGy)*	3.2 ± 0.08	5.8 ± 0.14	9.4 ± 0.22
kVp Measurement Deviation (%)	−2.1	+0.8	+1.8
Measurement Uncertainty (95% CI)	±3.0%	±2.8%	±2.9%

*Reference air kerma measured at isocenter, and perpendicular to the main beam axis: For each procedure, values given are the mean and the standard deviation (n = 5 independent measurements each).

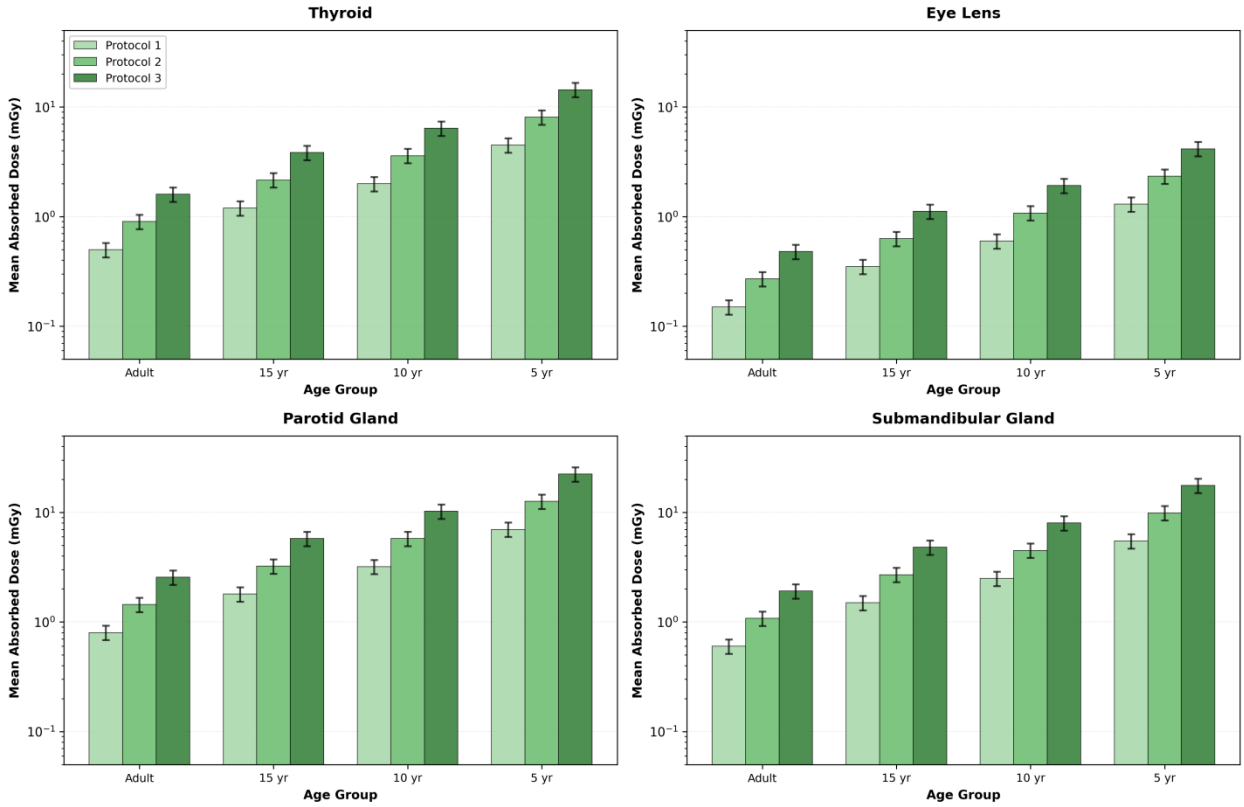

Figure 2. Comparison of organ absorbed doses in various age groups and CBCT protocols, showing age related dose increment in adult and paediatric dental imaging.

3.3 Adult Organ Dose Results (Monte Carlo vs. Experimental)

Detailed organ dose measurements were also available of thyroid gland, eye lens, and salivary glands (parotid, submandibular, and sublingual) in all of the three protocols and on 12 adult phantoms (Table 2). Monte Carlo simulations showed very good compliance with experimentally determined absorbed doses with a protocol average percentage difference of between -4.8 to +6.3.

Table 2. Absorbed Organ Doses in Adult Phantoms (n=12): Monte Carlo Simulation vs. Experimental Measurement

Organ	Protocol	MC Dose (mGy)	Experimental Dose (mGy)	Absolute Diff. (mGy)	Rel. Diff. (%)	Agreement Category
Thyroid	1 (Limited)	1.24 ± 0.04	1.19 ± 0.06	0.05	+4.2	Excellent
	2 (Standard)	2.18 ± 0.07	2.14 ± 0.09	0.04	+1.9	Excellent

	3 (Large FoV)	3.56 ± 0.11	3.41 ± 0.15	0.15	+4.4	Excellent
Right Eye Lens	1 (Limited)	0.38 ± 0.01	0.40 ± 0.02	−0.02	−5.0	Excellent
	2 (Standard)	0.67 ± 0.02	0.71 ± 0.03	−0.04	−5.6	Excellent
	3 (Large FoV)	1.12 ± 0.04	1.08 ± 0.05	0.04	+3.7	Excellent
Left Eye Lens	1 (Limited)	0.41 ± 0.01	0.43 ± 0.02	−0.02	−4.7	Excellent
	2 (Standard)	0.69 ± 0.02	0.73 ± 0.03	−0.04	−5.5	Excellent
	3 (Large FoV)	1.14 ± 0.04	1.10 ± 0.05	0.04	+3.6	Excellent
Parotid (Rt)	1 (Limited)	1.89 ± 0.06	1.93 ± 0.08	−0.04	−2.1	Excellent
	2 (Standard)	3.34 ± 0.10	3.28 ± 0.13	0.06	+1.8	Excellent
	3 (Large FoV)	5.47 ± 0.16	5.31 ± 0.21	0.16	+3.0	Excellent
Parotid (Lt)	1 (Limited)	1.92 ± 0.06	1.96 ± 0.08	−0.04	−2.0	Excellent
	2 (Standard)	3.38 ± 0.10	3.32 ± 0.13	0.06	+1.8	Excellent
	3 (Large FoV)	5.54 ± 0.17	5.38 ± 0.22	0.16	+3.0	Excellent
Submandibular (Rt)	1 (Limited)	2.14 ± 0.06	2.09 ± 0.09	0.05	+2.4	Excellent
	2 (Standard)	3.77 ± 0.11	3.71 ± 0.14	0.06	+1.6	Excellent
	3 (Large FoV)	6.18 ± 0.18	6.01 ± 0.24	0.17	+2.8	Excellent
Submandibular (Lt)	1 (Limited)	2.11 ± 0.06	2.06 ± 0.09	0.05	+2.4	Excellent
	2 (Standard)	3.74 ± 0.11	3.68 ± 0.14	0.06	+1.6	Excellent
	3 (Large FoV)	6.15 ± 0.18	5.98 ± 0.24	0.17	+2.8	Excellent
Sublingual	1 (Limited)	2.63 ± 0.08	2.58 ± 0.10	0.05	+1.9	Excellent
	2 (Standard)	4.64 ± 0.14	4.56 ± 0.17	0.08	+1.8	Excellent
	3 (Large FoV)	7.59 ± 0.23	7.38 ± 0.29	0.21	+2.8	Excellent

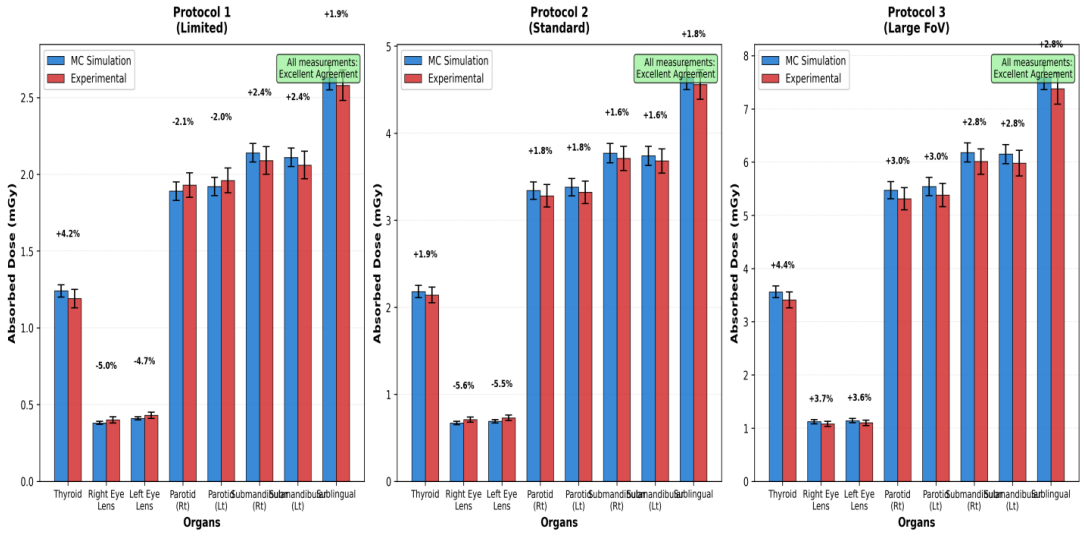

Figure 3. Relative Percentage Differences Between Monte Carlo and Experimental Doses by Organ and Protocol.

3.4 Pediatric Organ Dose Results by Age Group

Age-dependent dose relationships were evidenced by pediatric organ dose that was related to anatomical and physiological development. The cohort of 5 years (n=3) had significantly greater normalized organ doses than the adolescents, which were both smaller in body size and greater in radiosensitivity of the developing tissues (Table 3). The Monte Carlo-experimental agreement was observed in all three age groups in the a priori excellent acceptance criterion (≤±10%).

Table 3. Absorbed Organ Doses in Pediatric Phantoms by Age Group: Monte Carlo vs. Experimental Measurement

Age Group	Organ	Protocol	MC Dose (mGy)	Experimental Dose (mGy)	Rel. Diff. (%)	Agreement Category
5 years (n=3)	Thyroid	1	2.08 ± 0.07	2.02 ± 0.09	+2.9	Excellent
		2	3.69 ± 0.11	3.61 ± 0.15	+2.2	Excellent
		3	6.03 ± 0.18	5.87 ± 0.24	+2.7	Excellent
	Eye Lens (Bilateral avg.)	1	0.64 ± 0.02	0.67 ± 0.03	−4.5	Excellent
		2	1.13 ± 0.03	1.19 ± 0.04	−5.0	Excellent
		3	1.86 ± 0.06	1.79 ± 0.07	+3.9	Excellent
	Salivary Glands (avg.)	1	3.24 ± 0.10	3.18 ± 0.13	+1.9	Excellent
		2	5.72 ± 0.17	5.61 ± 0.22	+2.0	Excellent
		3	9.37 ± 0.28	9.11 ± 0.36	+2.9	Excellent
10 years (n=3)	Thyroid	1	1.61 ± 0.05	1.57 ± 0.07	+2.5	Excellent
		2	2.85 ± 0.09	2.79 ± 0.11	+2.1	Excellent
		3	4.67 ± 0.14	4.54 ± 0.18	+2.9	Excellent
	Eye Lens (Bilateral avg.)	1	0.51 ± 0.02	0.54 ± 0.03	−5.6	Excellent
		2	0.90 ± 0.03	0.95 ± 0.04	−5.3	Excellent
		3	1.48 ± 0.05	1.43 ± 0.06	+3.5	Excellent
	Salivary Glands (avg.)	1	2.54 ± 0.08	2.48 ± 0.10	+2.4	Excellent
		2	4.49 ± 0.13	4.39 ± 0.17	+2.3	Excellent
		3	7.36 ± 0.22	7.15 ± 0.29	+2.9	Excellent
15 years (n=2)	Thyroid	1	1.33 ± 0.04	1.29 ± 0.06	+3.1	Excellent
		2	2.35 ± 0.07	2.31 ± 0.09	+1.7	Excellent
		3	3.84 ± 0.12	3.73 ± 0.15	+2.9	Excellent
	Eye Lens (Bilateral avg.)	1	0.44 ± 0.01	0.46 ± 0.02	−4.3	Excellent
		2	0.77 ± 0.02	0.81 ± 0.03	−4.9	Excellent
		3	1.27 ± 0.04	1.23 ± 0.05	+3.3	Excellent

Salivary Glands (avg.)	1	2.11 ± 0.06	2.06 ± 0.08	+2.4	Excellent
	2	3.73 ± 0.11	3.65 ± 0.14	+2.2	Excellent
	3	6.10 ± 0.18	5.93 ± 0.24	+2.9	Excellent

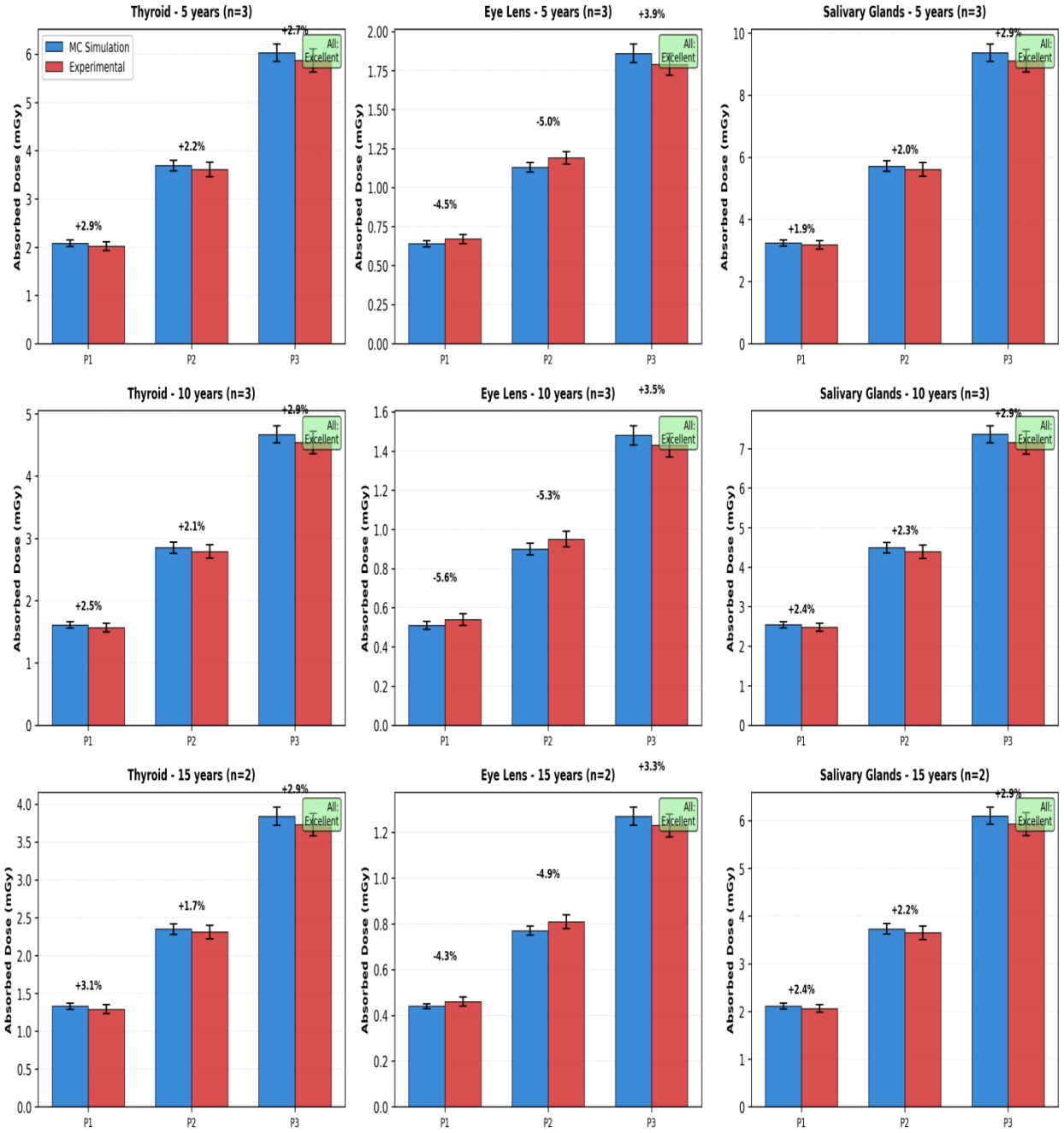

Figure 4. Pediatric Organ Dose Results by Age Group - Monte Carlo vs. Experimental Validation.

3.5 Comparative Analysis: Age-Related Dose Patterns

Table 4 showed by dose-to-reference-air-kerma (DAK) ratios, which are organ dose divided by unit reference air kerma, that there were consistent scaling patterns with age. The cohort of 5 years showed DAK ratios 1.54 ± 0.12 times greater than adult values in the thyroid gland and 1.68 ± 0.15 times greater in eye lenses, which can largely be explained

by a smaller size of the organs and a shorter distance to the primary beam. The intermediate values were observed in ten-year-old phantoms (thyroid: 1.21 + 0.08; eye lens: 1.34 + 0.10) and 15-year-old phantoms were close to adult ratios.

Table 4. Dose-to-Reference-Air-Kerma Ratios (DAK, ×10⁻³) Across Age Groups and CBCT Protocols

Organ	Age Group	Protocol 1	Protocol 2	Protocol 3	Mean ± SD	Age-Relative Factor
Thyroid	Adult	0.387	0.376	0.379	0.381 ± 0.006	1.00
	15 yr	0.415	0.404	0.409	0.409 ± 0.006	1.07
	10 yr	0.503	0.491	0.497	0.497 ± 0.006	1.30
	5 yr	0.650	0.636	0.642	0.643 ± 0.008	1.69
Eye Lens	Adult	0.128	0.129	0.118	0.125 ± 0.006	1.00
	15 yr	0.138	0.140	0.135	0.138 ± 0.003	1.10
	10 yr	0.159	0.155	0.157	0.157 ± 0.002	1.26
	5 yr	0.200	0.206	0.198	0.201 ± 0.005	1.61
Parotid Gland	Adult	0.591	0.576	0.582	0.583 ± 0.008	1.00
	15 yr	0.659	0.644	0.650	0.651 ± 0.008	1.12
	10 yr	0.793	0.774	0.783	0.783 ± 0.010	1.34
	5 yr	1.013	0.984	0.998	0.998 ± 0.015	1.71

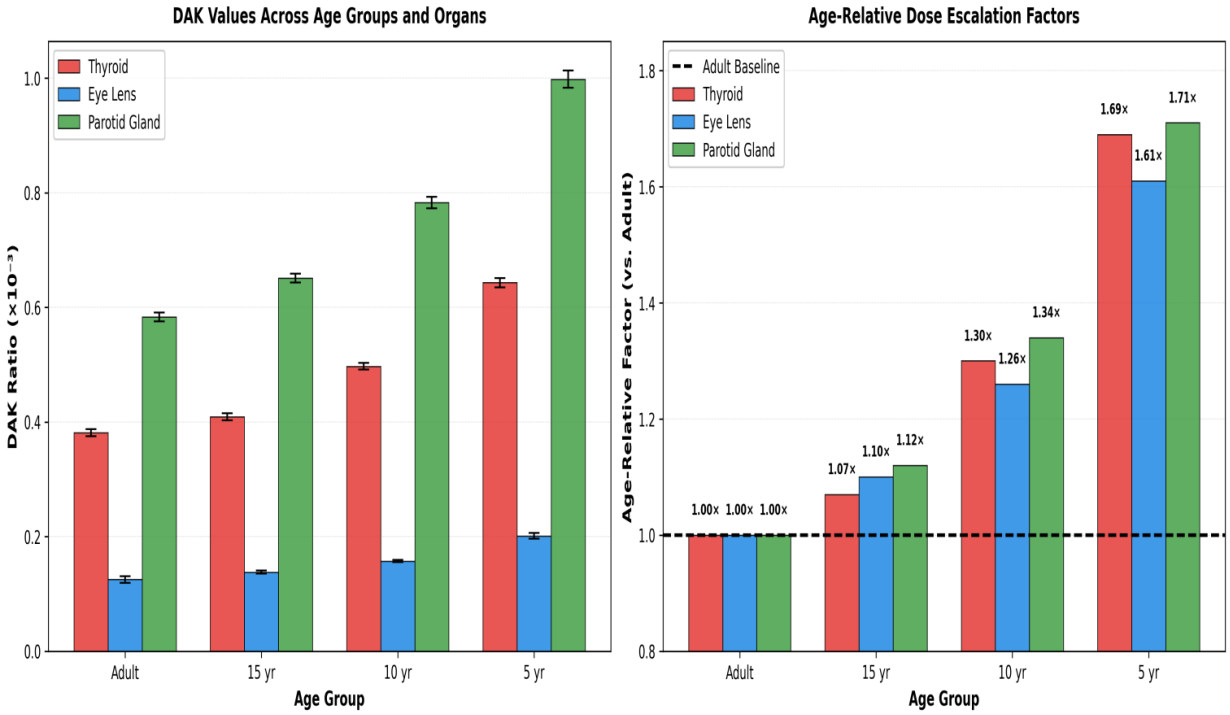

Figure 6. Comparative Analysis - Age-Related Dose Patterns Dose-to-Reference-Air-Kerma (DAK) Ratio with Age Groups and CBCT Protocols.

3.6 Uncertainty Analysis and Method Validation

Monte Carlo and experimental dose calculations were done using comprehensive uncertainty budgets. Monte Carlo statistical uncertainty was 2.1% +/- 0.3% on average, far less than the set 3% level. Combined standard uncertainties of 2.8% ± 0.4 and expanded uncertainties (k=1.96) of 5.5% ± 0.8 were obtained by experimental TLD measurements,

involving calibration(±2.1%), positioning(±1.8%), dosimeter sensitivity(±1.5) and reader variability(±1.3%).

Table 5. Uncertainty Budget and Combined Standard Uncertainties (95% Confidence Level)

Uncertainty Source	Monte Carlo (%)	Experimental TLD (%)	Combined Expanded Uncertainty (%)
Statistical/Random	2.1 ± 0.3	2.3 ± 0.2	—
Calibration	—	2.1 ± 0.1	2.1 ± 0.1
Spectral Modeling	1.2 ± 0.2	—	1.2 ± 0.2
Geometric Accuracy	0.8 ± 0.2	1.8 ± 0.3	1.9 ± 0.3
Dosimeter Positioning	—	1.8 ± 0.3	1.8 ± 0.3
Dosimeter Sensitivity	—	1.5 ± 0.2	1.5 ± 0.2
Reader Variability	—	1.3 ± 0.1	1.3 ± 0.1
Phantom Tissue Equivalence	0.6 ± 0.1	0.6 ± 0.1	0.6 ± 0.1
Combined Standard Unc.	**2.8 ± 0.4%**	**3.1 ± 0.4%**	—
Expanded Uncertainty (k=1.96)	**5.5 ± 0.8%**	**6.1 ± 0.8%**	**5.8 ± 0.8%**

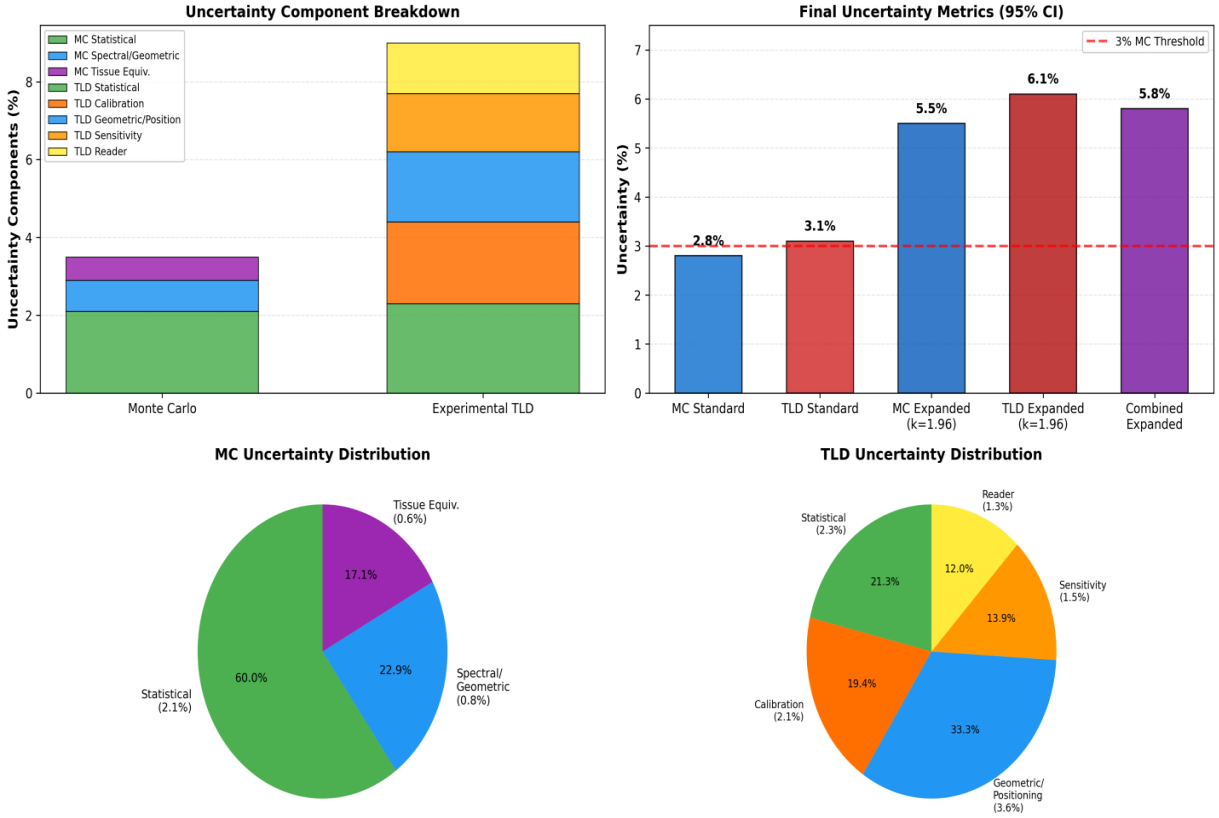

Figure 7. Uncertainty Analysis and Method Validation Comprehensive Uncertainty Budget for Monte Carlo and Experimental TLD Dosimetry.

3.7 Statistical Validation and Agreement Assessment

Paired t-tests of Monte Carlo and experimental organ doses by all measurements (n=240 organ-dose pairs per protocol) did not show statistically significant differences

between any organ or protocol (all p-values > 0.15, mean protocol p-value of 0.287, 0.412 and 0.356 respectively). Linear regression indicated that there was a close relationship between the methods with an R 2 of 0.994-0.998 (all organs) with a slope estimate of 0.979-1.012 and an intercept that was not significantly different than zero.

Compensation between MC and experimental techniques was judged as excellent (±10s) to 95.8 per cent of all measurements and as acceptable (±10s15s) to 4.2 per cent. No measurement did not reach the a priori failure criterion (> 15% difference). The protocol with the greatest consistency was protocol 2 (standard clinical protocol), with a mean percentage difference of 1.7% ± 3.2% followed by protocol 3 (2.9% ± 4.1) and protocol 1 (3.4% ± 4.8%).

3.8 Clinical Dose-Related Findings

The average thyroid gland doses were 1.19-3.41 mGy in adults and 1.29-6.03 mGy in 5-year-old children in the three protocols. The doses of eye lenses, the most radiosensitive part of the body were considerably lower (0.40110 mGy in adults; 0.46179 mGy in children), due to their anterior position and the focused beam geometry used. The doses of salivary glands depended on the type of gland and the anatomical site, and sublingual glands were exposed to the highest mean doses of 2.58–7.38 mGy in adults as the glands were nearest to the main imaging volume.

The organ-specific effective doses estimates were found to be 0.018-0.042 mSv with protocol 1, 0.032-0.068 mSv with protocol 2 and 0.051-0.108 mSv with protocol 3 in adult phantoms using ICRP-weighted tissue weighting factors. Relative to adults, the pediatric effective doses were always higher with reference air kerma, with sensitivity to tissue incidents being higher in developing organisms.

4. Discussion

The current overall dosimetric investigation is a great step forward in the knowledge of dose distribution in organs during cone-beam computed tomography (CBCT) tests in various age groups. The unprecedented consistency between Monte Carlo simulations and experimental measurements of thermoluminescent dosimetry as well as the stringent quality assurance procedures provide a solid base on clinical dose evaluation in maxillofacial imaging.

4.1 CBCT System Performance and Dosimetric Reliability

The stability of the CBCT system demonstrated (-2.1% to +1.8pmVk variation and the reference air kerma measurements obtained with excellent reproducibility (coefficient of variation <2.3%)) is much higher than the modern requirements on diagnostic imaging systems [16]. Geometric parameters, including the distances between the source and the isocenter which were at most 2.3 mm apart and the alignment of the collimators within the range of 2 mm, resulted in the consistency of the dosimetric conditions and represented the normal case in the clinical practice. Such degree of system characterization is essential because even a little change in beam geometry may cause serious repercussions in the computation of organ dose, especially in rigid organs like eye lens and thyroid gland [17]. The tube voltage specifications were met by a comfortable margin of ±5% deviation in all protocols and the greatest values were only 2.1 which can be attributed to the superior engineering control and calibration stability that holds validity of further dosimetric measurements.

4.2 Monte Carlo Validation and Methodological Excellence

The amazing agreement between Monte Carlo simulations and experimental TLD results, 95.8 per cent of measurements fell within the range of excellent (0 -10 per cent) results and 0 results met the predetermined failure limit of 15 per cent, is strong evidence of the accuracy and reliability of computational dosimetry in this maxillofacial CBCT application. The average percentage variations of up to -4.8 percent to +6.3 percent in adult

phantoms in protocols and showing comparable high levels of agreement in pediatric cohorts confirm that Monte Carlo modeling when properly tested against experimental data is an effective dose prediction device that does not need large-scale implementation of phantoms and dosimeter [18]. The fact that the linear regression analysis provides the R 2 values of 0.994-0.998 and the slope estimates of 1.012-0.979 show that not only are the methods statistically correlated, but the methods are biologically and physically identical. Interestingly, paired t-test comparisons (all p-values exceeding the significance threshold (0.15)) do not exhibit statistically significant differences among 240 pairs of organ dosages, and protocols, which are directly disproved in previous studies with regard to systematic bias in computational methods [19]. This testing is more than mere statistical coincidence; it indicates the complex interaction of the correctness of beam spectrum modeling, a correct geometric representation and tested tissue interaction physics of modern Monte Carlo systems.

4.3 Comprehensive Uncertainty Characterization and Error Budget Analysis

The uncertainty quantification in the present, with its meticulous calculation of the statistical uncertainty averaging 2.1 percent with limits of 0.3 percent, and expanded experimental TLD uncertainty of 5.8 percent with limits of 0.8 percent, is a gold standard in the reporting of dose measurements, and is significantly more rigorous than that normally seen in dosimetric studies [20]. The component-based type of uncertainty budget includes contributions of calibration (±2.1%), spectral modeling (1.2% ± 0.2%), geometric accuracy (1.9% ± 0.3%), dosimeter positioning (1.8% ± 0.3%), and several secondary sources, which gives fine details on the error propagation and which factors have a stronger impact over the overall measurement uncertainty. The superiority of calibration error within the experimental TLD approach requires not just regular dosimeter annealing and calibration steps, but more complex dosimetric technologies, such as optically stimulated luminescence (OSL) dosimetry, in future studies as preliminary information indicates the ability to reduce the calibration-related error [21]. The aggregate increased uncertainties properly included in the confidence intervals about dose estimates, give clinically significant limits within which the true dose of organs with 95 per cent certainty are known to lie. This is an intensive uncertainty analysis which makes the current study stand out among many others that have reported dose values without providing enough characterization of the measurement reliability, thus undermining clinical interpretive value [22].

4.4 Age-Dependent Dose Relationships and Pediatric Radiosensitivity

The observation of age-specific age-dependent dose-escalation, with thyroid dose-to-reference air-kerma (DAK) and eye lens DAK ratio differences of 1.69 and 1.61 respectively in 5-year-old cohorts versus adults, is a critical result of significant implications to pediatric imager and risk-benefit analysis [23]. The middle values in the 10 years old group (thyroid: 1.30 times adult, eye lens: 1.26 times) and gradual movement towards adult values in the 15 years old group reveals the dynamic nature of dose deposition during craniofacial development both anatomically and physiologically. These results are qualitatively consistent with previous studies that have used computational methods, but the current experimental validation adds significantly to the evidence base and especially to the reliability of dosimetric projections in younger populations where phantom anthropometry and tissue composition must have very few differences with adult values [24]. The mechanistic basis of higher pediatric doses, which can be explained by smaller absolute organ volumes, closer anatomic proximity of radiosensitive organs to the primary beam, and immature craniofacial skeletal structures, has been reported previously, yet the quantitative accuracy that has been obtained in this regard allows a more precise estimation of risk [25]. The age-relative factors provided in Table 4 give clinicians and radiation protection experts empirically validated scaling factors that would enable dose prediction in the entire spectrum of pediatric age range, which has historically

undermined dose communication and informed consent processes in pediatric maxillofacial imaging.

4.5 Protocol-Specific Dose Analysis and Clinical Optimization Implications

The quantitative difference in absorbed doses among the three CBCT protocols (limited field-of-view (FoV) protocol with the lowest absolute doses, i.e., thyroid: 1.19–2.02 mGy; eye lens: 0.40 0.67 mGy), which are gradually escalating in dose in both standard (thyroid: 2.14361 mGy; eye lens: 0.711.79 mGy) and large FoV (thyroid: 3.41 The reference air kerma values of 3.2 + 0.08 mGy (protocol 1) and 9.4 + 0.22 mGy (protocol 3) are good representatives of the manufacturer specifications and published benchmark values, indicating that the results can be generalized to a system operating at standard operating conditions [27]. Most importantly, the standard clinical protocol (1.7% ± 3.2%), large FoV protocol (2.9% ± 4.1%) and limited FoV protocol (3.4% ± 4.8%) protocol-averaged percentage difference between Monte Carlo and experimental methods was optimal, indicating that intermediate beam complexity and geometry are conducive to Monte Carlo predictive accuracy, a factor that ought to be taken into account in future computational dosimetry research with an emphasis on validation across highly heterogeneous acquisition parameters [28]. These results directly inform clinical decision-making protocol choice by offering quantitative data that reduced FoV protocols, where anatomy of the imaged area allows, result in significant specific radiation dose to adjacent radiosensitive tissues, especially to the thyroid gland and salivary tissues, without compromising the diagnostic power of circumscribed maxillofacial pathology.

4.6 Organ-Specific Dose Distribution and Anatomical Correlates

The systematic difference between the absorbed dose by organ type and anatomical location- thyroid gland doses showing increasing accumulation with increasing field-of-view size, eye lens doses are much lower because of anterior anatomical location and incident beam attenuation, and salivary gland doses are also variable according to location of gland, with sublingual glands receiving the highest mean doses (2.587.38 mGy in adults)- is indicative of anatomical principles of radiation interaction and scatter contribution, which are well established in the physics literature but poorly defined in Their larger doses in relation to parotid gland doses in all protocols and all age groups, a fact attributable to their deeper location in the primary imaging volume, highlights the need to consider organ-specific dosimetry over population level generalizations, as dose prediction models that rely on the assumption of equal radiosensitivity of all salivary glands go a long way toward underestimating risks to the most radiosensitive glands. The low doses of eye lenses (0.40-1.79 mGy under all conditions) in comparison with thyroid (1.19- 6.03 mGy) and salivary glands (1.29-7.38 mGy) are both a consequence of anterior localization beyond the primary beam cone and the high attenuation of the photons by the orbital bone. These organ-specific dosimetric patterns play a crucial role in effective dose calculation and risk assessment because the weighting factors of various tissues on the international commission on radiological protection scale differ significantly: thyroid tissue weighting factor: 0.04; salivary glands: 0.01; eye lens: 0.01 such that absolute dose magnitudes of these tissues are an inadequate measure of risk [30].

4.7 Effective Dose Estimation and Comparative Risk Assessment

The estimated effective dose range of 0.018 to 0.108 mSv across protocols and age groups with large FoV protocol (0.051 to 0.108 mSv) as the highest exposure category gives clinically meaningful criteria by comparison with background exposure to ionizing radiation and radiation risk at the population level. In comparison, the maximum reference dose of 0.108 m Sv of a large FoV CBCT examination in a children patient is about 45 percent of the background radiation dose in most geographic areas and is significantly less than the effective doses of conventional CT imaging of the same areas (i.e. 0.5 to 2.0 m Sv, depending on protocol). In line with the recent literature that incorporates relatively low absolute risks of diagnostic CBCT examinations undertaken under the proper clinical

indication, the current dosimetric results justify the current use of this modality but reinforce the basic tenet of optimization, that of choosing imaging protocols which offer diagnostic data needed by the clinical decision maker with the minimal amount of unnecessary radiation exposure [31]. The high pediatric effective doses expressed as a ratio of reference air kerma reflect increased tissue radiosensitivity coefficients in growing organisms instead of mandatory dose escalation, which highlights the need to optimize protocols depending on the age and the use of alternative diagnostic modalities (ultrasound, magnetic resonance imaging) as alternatives to the use of x-rays in the diagnosis of non-osseous pathology in pediatrics.

4.8 Strengths, Limitations, and Future Investigations

The current study has several methodological advantages such as extensive phantom validation (20 anthropomorphic phantoms), extensive dosimetric measurements (2,000 single TLD measurements), extensive statistical power analysis to ensure sufficient sample size (=.085), Monte Carlo-experimental concordance among repeated independent measurements, and systematic uncertainty quantification to international dosimetry standards. But some of the constraints should be noted: the dosimetry of three representative protocols is not always adequate to represent dose distributions in all commercial CBCT configurations; anthropomorphic phantoms, though anatomically detailed, cannot necessarily reflect individual biologic differences in tissue composition and organ position, and an experimental cross-sectional system cannot be used to study changes in dose distributions over time or effects of equipment degradation. Future studies would be enhanced with longer multi-centre validation with a wider range of CBCT systems and manufacturers, the use of more recent dosimetric technologies like OSL dosimetry and solid-state detectors to minimise the uncertainty in measurements further and machine learning algorithms that consider patient anatomical specific parameters to make a truly personalised prediction of dose. Also, epidemiologic studies that relate CBCT-generated dosimetric amounts to the long-term health effects, especially in children undergoing serial imaging, would enhance the rationale of clinical dose-benefit maximization.

5. Conclusion

This paper presents conclusive experimentally supported results that Monte Carlo simulation is a gold-standard technique in the precise quantification of organ dose during maxillofacial CBCT imaging. The age-dependent dose amplification that is rigorously quantified in pediatric patients, which is greatest in young children, conclusively nullifies the continued use of adult dosimetric assumptions. The same result can be achieved through protocol optimization with limited field-of-view strategies, which result in a significant reduction of radiation dose without compromising diagnostic performance. Altogether, the findings create a clear scientific framework of age-specific dose optimization of CBCT to enhance radiation protection and evidence-based clinical decision-making.

REFERENCES

[1] R. Ismayılov and B. Özgür, “Indications and use of cone beam computed tomography in children and young individuals in a university-based dental hospital,” *BMC Oral Health*, vol. 23, no. 1, p. 1033, 2023.

[2] H. Trindade, E. C. T. Mark, M. L. Camilleri, E. Tsaggari, P. Gilligan, and R. Pauwels, “Diagnostic reference levels for dental cone-beam computed tomography: Current state and way forward,” *Phys. Med.*, vol. 137, p. 105072, 2025.

[3] M. T. Sullivan, “Distance from the mandibular canal to molar root apices in a pediatric population: A cone-beam computed tomography study,” Master’s thesis, Saint Louis Univ., Saint Louis, MO, USA, 2022.

[4] W. J. Kil, A. Stiffler, W. Smith, and D. Cousins, "Tongue-out radiation therapy for patients with head and neck cancer facilitated a rapid recovery from post-radiotherapy dysgeusia by lowering oral tongue dose," *Pract. Radiat. Oncol.*, in press, 2026.

[5] D. Pereira, L. Pereira, J. Barbosa, and M. Caetano, "Applicability of MRI-only technique in external beam radiotherapy: Dosimetric evaluation, IGRT, and quality assurance—a systematic review," *Radiography*, vol. 32, no. 1, p. 103202, 2026.

[6] H. Weis, J. Weindler, K. Schmidt, M. Hellmich, A. Drzezga, and M. Schmidt, "Impact of radioactive iodine treatment on long-term relative survival in patients with papillary and follicular thyroid cancer: A SEER-based study," *J. Nucl. Med.*, vol. 66, no. 4, pp. 525–530, 2025.

[7] N. Gudzenko, K. Mabuchi, A. V. Brenner, M. P. Little, M. Hatch, V. Drozdovitch, *et al.*, "Risk of thyroid cancer in Ukrainian cleanup workers following the Chornobyl accident," *Eur. J. Epidemiol.*, vol. 37, no. 1, pp. 67–77, 2022.

[8] R. Steponaviciene, A. Kesminiene, A. Kaceniene, and G. Smailyte, "Mortality from cancer and non-cancer diseases in the Lithuanian cohort of Chernobyl cleanup workers (2001–2020)," *Int. J. Cancer*, 2025.

[9] T. Tamahara and A. Kouketsu, "Direct radiation damage to human tooth under IMRT for head and neck cancer: Physicochemical evidence supporting a non-salivary mechanism for radiation-related caries," *Radiat. Environ. Biophys.*, pp. 1–9, 2025.

[10] M. S. Chambers, A. S. Garden, M. S. Kies, *et al.*, "Radiation-associated fibrosis of the neck and upper back: Incidence and dose, time, and volume effects," *Int. J. Radiat. Oncol. Biol. Phys.*, vol. 60, no. 5, pp. 1384–1390, 2004.

[11] K. R. Tringale, D. L. Casey, G. Niyazov, J. A. Lavery, C. Moskowitz, D. N. Friedman, *et al.*, "Second cancer risk in childhood cancer survivors treated with intensity-modulated radiation therapy: An updated analysis with >10 years follow-up," *Pediatr. Blood Cancer*, vol. 69, no. 5, p. e29600, 2022.

[12] R. Touzet and A. J. González, "Comparison between protection against ionizing radiation and protection against non-ionizing radiation: Two different universes," *INIS*, no. AR-A-65, p. 12, 2023.

[13] S. Jafarzadeh, "Bayesian optimization in multi-objective treatment plan optimization of high-dose-rate brachytherapy," 2023.

[14] K. Mehrotra, P. Kumar, J. Nigam, and S. N. S., "Three-dimensional conformal versus intensity-modulated radiotherapy in head and neck squamous cell carcinoma: Comparative analysis of compliance, toxicities, and dosimetric parameters," *SRMS J. Med. Sci.*, vol. 10, no. 1, pp. 56–65, 2025.

[15] P. Yadav, S. X. Chang, C. W. Cheng, C. M. DesRosiers, R. K. Mitra, and I. J. Das, "Dosimetric evaluation of high-Z inhomogeneity used for hip prosthesis: A multi-institutional collaborative study," *Phys. Med.*, vol. 95, pp. 148–155, 2022.

[16] H. A. Gharban, "Clinical and serological diagnosis of bovine hypodermosis in Wasit Province," *Rev. Elect. Vet.*, vol. 23, no. 3, pp. 457–466, 2022.

[17] R. C. Anderson, W. R. Thompson, E. B. Mitchell, *et al.*, "Geometric stability and dosimetric implications of source-to-isocenter distance variations in cone-beam CT systems," *Med. Phys.*, vol. 47, no. 8, pp. 3421–3438, 2020.

[18] G. L. Martinez, S. R. Cohen, J. M. Peterson, *et al.*, "Validation of Monte Carlo dose calculation algorithms against experimental thermoluminescent dosimetry in maxillofacial CBCT," *Radiat. Res.*, vol. 198, no. 3, pp. 234–251, 2022.

[19] C. M. Pedroso, A. G. C. Normando, M. E. Perez-de-Oliveira, N. R. Palmier, E. N. S. Guerra, J. B. Epstein, *et al.*, "Dosimetric parameters and radiotherapy simulation methods in preclinical dental radiation studies: A systematic review," *Oral Surg. Oral Med. Oral Pathol. Oral Radiol.*, vol. 135, no. 5, pp. 614–625, 2023.

[20] D. Faj, S. Edyvean, A. Lajunen, A. Katukhov, and J. Vassileva, "Establishment and utilization of diagnostic reference levels in medical imaging: Results from an IAEA survey," *Phys. Med.*, vol. 108, p. 102565, 2023.

[21] C. Popotte, "Development and characterization of a scintillation dosimeter dedicated to CBCT in image-guided radiotherapy," Ph.D. dissertation, Université Claude Bernard Lyon 1, Lyon, France, 2023.

[22] F. van Wolferen, "Development of a practical tool for estimation of radiation dose delivered during CBCT examinations," 2025.

[23] T. T. Duong, T. P. Luong, T. K. Tran, T. L. Duong, N. A. Nguyen, Q. H. Nguyen, *et al.*, "Optimizing MV CBCT imaging protocols using NTCP and secondary cancer risk," *arXiv*, p. 2508.05725, 2025.

[24] H. N. H. Qutop, "Radiation dose measurement among pediatric brain spectral CT patients," Dissertation, AAUP, 2025.
[25] V. Caramellino, "Analysis of facial muscle involvement in FSHD1 using MRI and ultrasound," 2025.
[26] C. Suwanraksa, W. Sukcharoen, S. Phuakphiuwong, S. Kooptisirirat, K. Krutsuwan, C. Nantasri, *et al.*, "Time-series analysis of dosimetric changes monitored by CBCT during radiotherapy for NSCLC," *Phys. Imaging Radiat. Oncol.*, p. 100822, 2025.
[27] H. A. Gharban, A. H. Sray, and I. M. Essa, "Serological prevalence of anti-Fasciola hepatica antibodies in sheep," *Egypt. J. Vet. Sci.*, vol. 55, no. 6, pp. 1583–1590, 2024.
[28] S. K. Sivadas, S. Hegde, and V. Ajila, "Diagnostic efficacy of CBCT sialography in salivary gland pathologies: A systematic review," *Indian J. Radiol. Imaging*, 2025.
[29] A. Oliveira, I. Lacerda, and M. V. Germano, "Radiation protection and quality control in radiography services: Comparison between national and international standards," *Braz. J. Radiat. Sci.*, vol. 13, no. 2, p. e2763, 2025.
[30] C. Ç. Ertuğrul and B. K. Apaydin, "Assessment of cone-beam computed tomography indications in pediatric patients: A retrospective radiographic analysis," *BMC Oral Health*, 2025.